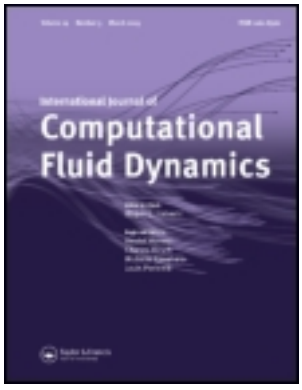

International Journal of Computational Fluid Dynamics
Publication details, including instructions for authors and subscription information:
http://www.tandfonline.com/loi/gcfd20

Effect of confinement on droplet deformation in shear flow

Haobo Hua[a], Yibao Li[b], Jaemin Shin[a], Ha-kyu Song[a] & Junseok Kim[a]
[a] Department of Mathematics, Korea University, Seoul 136-713, Republic of Korea
[b] Department of Computational Science and Engineering, Yonsei University, Seoul 120-749, Republic of Korea
Published online: 12 Nov 2013.

To cite this article: Haobo Hua, Yibao Li, Jaemin Shin, Ha-kyu Song & Junseok Kim (2013) Effect of confinement on droplet deformation in shear flow, International Journal of Computational Fluid Dynamics, 27:8-10, 317-331, DOI: 10.1080/10618562.2013.857406

To link to this article: http://dx.doi.org/10.1080/10618562.2013.857406

International Journal of Computational Fluid Dynamics, 2013
Vol. 27, Nos. 8–10, 317–331, http://dx.doi.org/10.1080/10618562.2013.857406

RESEARCH ARTICLE

Effect of confinement on droplet deformation in shear flow

Haobo Hua[a], Yibao Li[b], Jaemin Shin[a], Ha-kyu Song[a] and Junseok Kim[a,*]

[a]*Department of Mathematics, Korea University, Seoul 136-713, Republic of Korea;* [b]*Department of Computational Science and Engineering, Yonsei University, Seoul 120-749, Republic of Korea*

(*Received 21 September 2012; accepted 14 October 2013*)

The dynamics of a single droplet under shear flow between two parallel plates is investigated by using the immersed boundary method. The immersed boundary method is appropriate for simulating the drop-ambient fluid interface. We apply a volume-conserving method using the normal vector of the surface to prevent mass loss of the droplet. In addition, we present a surface remeshing algorithm to cope with the distortion of droplet interface points caused by the shear flow. This mesh quality improvement in conjunction with the volume-conserving algorithm is particularly essential and critical for long time evolutions. We study the effect of wall confinement on the droplet dynamics. Numerical simulations show good agreement with previous experimental results and theoretical models.

Keywords: wall effect; immersed boundary method; shear flow; volume conserving; remeshing; droplet deformation

1. Introduction

Deformation and breakup of droplets play an important role in the morphological development of blends (Tucker III and Moldenaers 2002) as can be seen from their applications in industry and natural processes such as in emulsions, ink-jet printers, oil recovery and biological cell systems. Let us consider two immiscible fluids, with a droplet of one fluid surrounded by another ambient fluid with a Newtonian viscosity η and interfacial tension coefficient σ. There are two main parameters that determine the deformation and breakup behaviour of the droplet component: the capillary number Ca and the viscosity ratio λ. The capillary number is defined as $Ca = \eta_m R\dot{\gamma}/\sigma$, where η_m, R and $\dot{\gamma}$ denote the viscosity of the ambient fluid, the radius of the undeformed droplet, and the shear rate, respectively. The capillary number expresses the ratio between viscous stresses that distort the droplet shape and interfacial stresses that restore the droplet shape. The viscosity ratio is defined as the ratio of the droplet viscosity to the ambient fluid viscosity: $\lambda = \eta_d/\eta_m$, where η_d is the droplet viscosity.

The degree of confinement or confinement ratio is defined as the ratio of the droplet diameter to the distance between two parallel plates. After the pioneering research on the dynamics of small droplets immersed in another fluid by Taylor (1932, 1934), most investigations have concentrated on the unconfined droplet deformation and breakup experimentally and theoretically (Chaffey and Brenner 1967; Rallison 1984). Several reviews are available in the literature (Stone 1994; Tucker III and Moldenaers 2002; Cristini and Renardy 2006). For the numerical simulation of the droplet dynamics, a number of different methodologies have been developed, including the volume-of-fluid (Gueyffier et al. 1999; Renardy and Cristini 2001; Renardy 2007), boundary-integral (Cristini et al. 2003; Janssen and Anderson 2007; Vananroye et al. 2008), phase-field (Yue et al. 2004; Kim 2005; Yue et al. 2006; Ceniceros, Nos, and Roma 2010), level set (Pillapakkam and Singh 2001; Xu et al. 2006; Ardekani, Dabiri, and Rangel 2009), and immersed boundary methods (IBM; Sheth and Pozrikidis 1995).

The desired droplet-size distribution in multiphase systems, which is important in industrial processes, has been studied (Thorsen et al. 2001; Tice, Lyon, and Ismagilov 2004; Garstecki, Stone, and Whitesides 2005). In these multiphase systems, the droplet diameter is typically of the order of the parallel plate height; therefore, wall effects play an important role on droplet deformation. Many experimental and numerical investigations on the behaviour of a single droplet especially under confined shear flow have been performed (Sibillo et al. 2006; Vananroye, Van Puyvelde, and Moldenaers 2006a, 2006b; Griggs, Zinchenko, and Davis 2007; Janssen and Anderson 2007; Renardy 2007; Vananroye, Van Puyvelde, and Moldenaers 2007; Cardinaels et al. 2011).

Janssen and Anderson (2007) studied the evolution of the shape of a single droplet placed between two parallel plates using the boundary-integral method. The authors investigated the influence of the capillary number and confinement ratio on droplet deformation. Vananroye et al. (2008) also used the boundary-integral method to compare

* Corresponding author. Email: cfdkim@korea.ac.kr

the experimental and numerical results. They predicted an increase in droplet deformation and greater orientation to the flow direction with the increase of the degree of confinement. Cardinaels et al. (2011) numerically investigated the effect of confinement on the droplet dynamics after startup of shear flow for systems with one viscoelastic component using the volume-of-fluid method. They found that confinement substantially increases the elongation rate in and around the droplet. Shapira and Haber (1988) gave a theoretical prediction of single droplet deformation at steady state under confined shear flow. Recently, Minale (2008) developed a phenomenological model, which is forced to recover the small deformation limits of Shapira and Haber (1990), successfully matching the experimental data available in the literature. See Minale (2010) for a review on the theoretical models for the deformation of a single ellipsoidal droplet.

In this paper, we focus on the investigation of the dynamics of droplet deformation with wall confinement. We use the IBM to study droplet dynamics. In general, the IBM does not guarantee the conservation of volume. Therefore, we apply the area-preserving method (Li et al. 2012) and volume-conserving method (Li et al. 2013) to overcome the lack of conservation in the IBM. In previous work (Li et al. 2013), however, there has been a limitation for the long-time evolution and large deformation because of mesh distortion. The goal of this paper is to incorporate a surface remeshing algorithm into the recently developed volume-conserving IBM (Li et al. 2013) for two-phase fluid flow. In this work, we apply the volume mesh generator DistMesh developed by Persson and Strang (2004) and Persson (2006) to remesh the distorted surface mesh.

The rest of the paper is organised as follows. In Section 2, we state the problem of droplet deformation in shear flow and introduce the mathematical formulations. In Section 3, we describe the numerical implementation of the remeshing algorithm, construction of the signed distance function and IBM. Sections 4 and 5 present numerical results in two and three dimensions, respectively. Finally, conclusions are drawn in Section 6.

2. Problem statement and governing equations

We consider the dynamical motion of a single droplet in an ambient fluid between two parallel plates as schematically depicted in Figure 1. The velocity vector field is generated by the boundary condition for $\mathbf{u} = (\pm\dot{\gamma}H, 0, 0)$ at $z = \pm H$, where H is the wall height and $\dot{\gamma}$ is the shear rate. For the x- and y-directions, we use a periodic boundary condition for the velocity $\mathbf{u}$. For the pressure variable, we impose a periodic boundary condition for the x- and y-directions and a zero-Neumann boundary condition for the z-direction. To measure the magnitude of the deformation, we use the Taylor deformation number defined by $D = (L - B)/(L + B)$, where L and B are, respectively, the major and minor

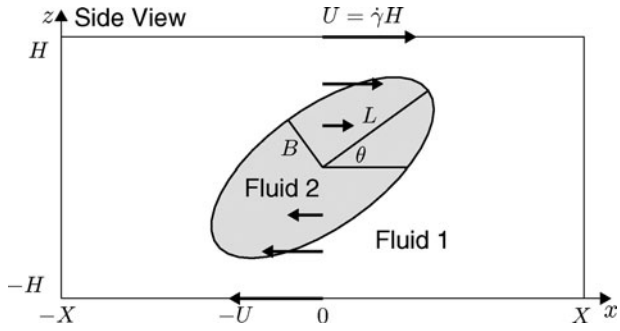

Figure 1. Schematic illustration for a liquid droplet (Fluid 2) in an ambient fluid (Fluid 1) under shear flow.

drop semiaxes in the x–z plane. W is another semiaxis in the x–y plane. The orientation angle θ is defined as the angle between the L-axis and the velocity direction.

The mathematical model is based on the IBM developed by Peskin (1977). Let the fluid velocity $\mathbf{u}(\mathbf{x}, t) = (u(\mathbf{x}, t), v(\mathbf{x}, t), w(\mathbf{x}, t))$ be defined on the fixed Cartesian coordinate $\mathbf{x} = (x, y, z)$ at time t. We denote $\mathbf{X}(t)$ as the Lagrangian variable for the immersed boundary. The Lagrangian variable $\mathbf{X}(t)$ separates the domain into two regions occupied by two distinct fluids. The fluid flow is computed in the whole domain and then $\mathbf{X}(t)$ is advected by the interpolated fluid velocity from $\mathbf{u}(\mathbf{x}, t)$. The fluid interacts with the boundary via singular forces exerted by the boundary. This surface tension force is spread to the surrounding Eulerian variable $\mathbf{x}$ using a delta function. We suppose that the density and viscosity are both constant. The dimensionless equations of motion for the system are as follows:

$$\frac{\partial \mathbf{u}(\mathbf{x}, t)}{\partial t} + \mathbf{u}(\mathbf{x}, t) \cdot \nabla \mathbf{u}(\mathbf{x}, t) = -\nabla p(\mathbf{x}, t) + \frac{1}{Re}\Delta \mathbf{u}(\mathbf{x}, t) + \frac{1}{We}\mathbf{f}(\mathbf{x}, t), \quad (1)$$

$$\nabla \cdot \mathbf{u}(\mathbf{x}, t) = 0, \quad (2)$$

$$\mathbf{f}(\mathbf{x}, t) = \int_{\Gamma} \mathbf{F}(\mathbf{X}(t))\delta(\mathbf{x} - \mathbf{X}(t))ds, \quad (3)$$

$$\mathbf{U}(\mathbf{X}(t)) = \int_{\Omega} \mathbf{u}(\mathbf{x}, t)\delta(\mathbf{x} - \mathbf{X}(t))d\mathbf{x}, \quad (4)$$

$$\frac{d\mathbf{X}(t)}{dt} = \mathbf{U}(\mathbf{X}(t)). \quad (5)$$

Here, Ω is the domain and Γ is the interface between the two fluids. The Reynolds number in Equation (1) is defined as $\mathrm{Re} = \rho_m R^2 \dot{\gamma}/\eta_m$, where ρ_m is the density of the ambient fluid. Then, the Weber number can be defined as $We = Re \cdot Ca$. The fluid velocity $\mathbf{u}(\mathbf{x}, t)$, pressure $p(\mathbf{x}, t)$, and singular surface tension force $\mathbf{f}(\mathbf{x}, t)$ are Eulerian variables in a Cartesian domain $\Omega \in \mathbb{R}^d$ ($d = 2$ or 3). The boundary force density $\mathbf{F}(\mathbf{X}(t))$ and boundary velocity $\mathbf{U}(\mathbf{X}(t))$ are

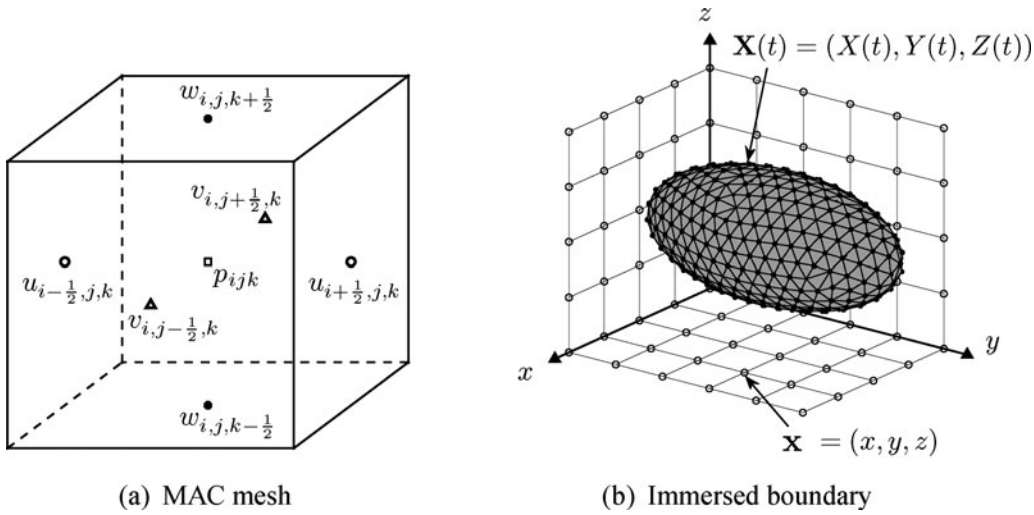

(a) MAC mesh (b) Immersed boundary

Figure 2. (a) Velocities defined at cell interfaces and pressure defined at the cell centres in three dimensions. (b) Illustration of Eulerian points $\mathbf{x}$ and Lagrangian points $\mathbf{X}(t)$. (a) MAC mesh. (b) Immersed boundary.

Lagrangian variables. $\mathbf{F}(\mathbf{X}(t))$ is defined as

$$\mathbf{F}(\mathbf{X}(t)) = \kappa(\mathbf{X}(t))\mathbf{n}(\mathbf{X}(t)), \tag{6}$$

where κ is the mean curvature and $\mathbf{n}$ is the unit outward normal vector. $\delta(\mathbf{x} - \mathbf{X}(t))$ is the Dirac delta function, which is defined by the product of one-dimensional Dirac delta functions, i.e. $\delta(\mathbf{x}) = \delta(x)\delta(y)$ and $\delta(\mathbf{x}) = \delta(x)\delta(y)\delta(z)$ in two and three dimensions, respectively.

3. Numerical implementation

In this section, we briefly describe the DistMesh algorithm and IBM in three dimensions. During the simulation of droplet deformation in shear flow by the IBM, the distribution of surface mesh could be seriously distorted. In a long time simulation, this distorted mesh distribution could lead to an inaccurate calculation of surface curvature. Eventually, the droplet shape will not well maintained. The rest of this section is devoted to explaining the algorithm for regenerating the surface mesh in conjunction with the volume-conserving IBM.

3.1. Discretisation

We discretise the domain $\Omega = (a, b) \times (c, d) \times (e, f)$ in three-dimensional space. Two-dimensional discretisation is analogously defined. Let a computational domain be partitioned into a uniform mesh with a space step size h in a Cartesian geometry. The center of each cell is located at $\mathbf{x}_{ijk} = (x_i, y_j, z_k)$, where $x_i = a + (i - 0.5)h$, $y_j = c + (j - 0.5)h$, and $z_k = e + (k - 0.5)h$, for $i = 1, \ldots, N_x, j = 1, \ldots, N_y$ and $k = 1, \ldots, N_z$. Here, N_x, N_y and N_z are the numbers of cells in the x-, y-, and z-directions, respectively.

Let u^n_{ijk} be an approximation of $u(x_i, y_j, z_k, t_n)$, where $t_n = n\Delta t$ and Δt is the time step size.

We use a staggered marker-and-cell mesh, in which pressure is stored at cell centres and velocities are stored at cell interfaces (Harlow and Welch 1965). Velocity components u, v, and w are defined at the x-, y-, and z-directional face centres, respectively (see Figure 2(a)). We use a set of M Lagrangian points $\mathbf{X}^n_l = (X^n_l, Y^n_l, Z^n_l)$ for $l = 1, \ldots, M$ to discretise the immersed boundary. There are M_T triangles $\mathbf{Tri}_s = (\mathbf{X}_l, \mathbf{X}_m, \mathbf{X}_q)$ for $s = 1, \ldots, M_T$ with the three vertices $\mathbf{X}_l$, $\mathbf{X}_m$ and $\mathbf{X}_q$ for each triangle being ordered counterclockwise (see Figure 2(b)).

3.2. DistMesh algorithm for the surface mesh

To generate the triangular surface mesh using the implicit representation of the surface, we use the DistMesh algorithm (Persson and Strang 2004; Persson 2006). Let us take a two-dimensional example to illustrate the basic idea of the algorithm. Let the interface of two fluids be implicitly represented as the zero-level set of an implicit function. For example, the function $\phi(x, y) = \sqrt{x^2 + y^2} - 1$ implicitly represents the unit circle by the zero level set $\phi = 0$, which is shown by the dashed curve in Figure 3. The main procedure for generating the triangular surface mesh is as follows (where, to simplify the explanation, we denote the node points at *Step 1* by $\mathbf{X}^{n,1}$. $\mathbf{X}^{n,2}$ and $\mathbf{X}^{n,3}$ are defined in a similar manner):

Step 1. Assign the repulsive force depending on the length of the edge of each triangle and calculate the net force at node points $\mathbf{X}^{n,1}$ (see Figure 3(a)).

Step 2. According to the net force, move node points $\mathbf{X}^{n,1}$ to $\mathbf{X}^{n,2}$ (see Figure 3(b)).

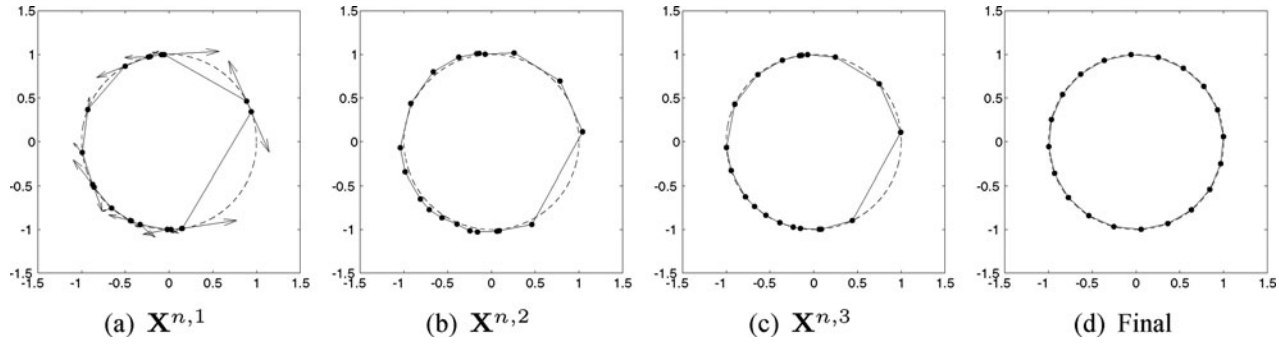

Figure 3. Surface mesh generation: (a) net force vectors, (b) triangulation after moving points, (c) projection to the interface, and (d) final triangulation. (a) $\mathbf{X}^{n,1}$. (b) $\mathbf{X}^{n,2}$. (c) $\mathbf{X}^{n,3}$. (d) Final.

Step 3. To get $\mathbf{X}^{n,3}$, project node points $\mathbf{X}^{n,2}$ to the zero-level contour with respect to the normal direction $|\nabla\phi|$ (see Figure 3(c)).

We repeat *Steps 1–3* until the mesh uniformity is satisfactory, i.e. until the movements of node points are less than a given tolerance (see Figure 3(d)). The projection step should be applied because points slightly deviate from the zero-level set by *Step 2*. To project the point $\mathbf{X}_l^{n,2}$ to the surface $\phi = 0$ at the *Step 3*, we use the first-order approximation

$$\mathbf{X}_l^{n,3} = \mathbf{X}_l^{n,2} - \phi\left(\mathbf{X}_l^{n,2}\right)\frac{\nabla\phi\left(\mathbf{X}_l^{n,2}\right)}{\left|\nabla\phi\left(\mathbf{X}_l^{n,2}\right)\right|^2}. \tag{7}$$

In the three-dimensional case, the above algorithm is not sufficient for the moving points to satisfy the mesh uniformity. To obtain a high-quality triangulation, we update the connectivity to maintain good triangulation of the nodes during the iterations. We only update the bad triangles by changing the local connectivity. In the flipping algorithm, we sweep all elements and consider flipping the edge between neighbouring triangles. For example, the triangles $\mathbf{Tri}_{s_1} = (\mathbf{X}_a, \mathbf{X}_b, \mathbf{X}_d)$ and $\mathbf{Tri}_{s_2} = (\mathbf{X}_a, \mathbf{X}_c, \mathbf{X}_b)$ in Figure 4(a) change to $\mathbf{Tri}_{s_1} = (\mathbf{X}_a, \mathbf{X}_c, \mathbf{X}_d)$ and $\mathbf{Tri}_{s_2} = (\mathbf{X}_c, \mathbf{X}_b, \mathbf{X}_d)$ in Figure 4(b).

3.3. *Signed distance function*

We use the surface mesh, which is the immersed boundary surface, to construct a signed distance function. The interface between two fluids is implicitly defined by using the signed distance function. Let us take a two-dimensional example to illustrate the basic idea of the method. We take 20 uniformly distributed points for a circle of radius 0.25 on the computational domain $(0, 1) \times (0, 1)$ discretised by a 32×32 mesh. Each element distributes the distance and orientation from itself to nearby points (see Figure 5(a)). At the point that receives data, we compare the receiving and existing distances, then choose the smaller one and its orientation. After all elements distribute data, we have the shortest distance and its orientation to the surface at a set

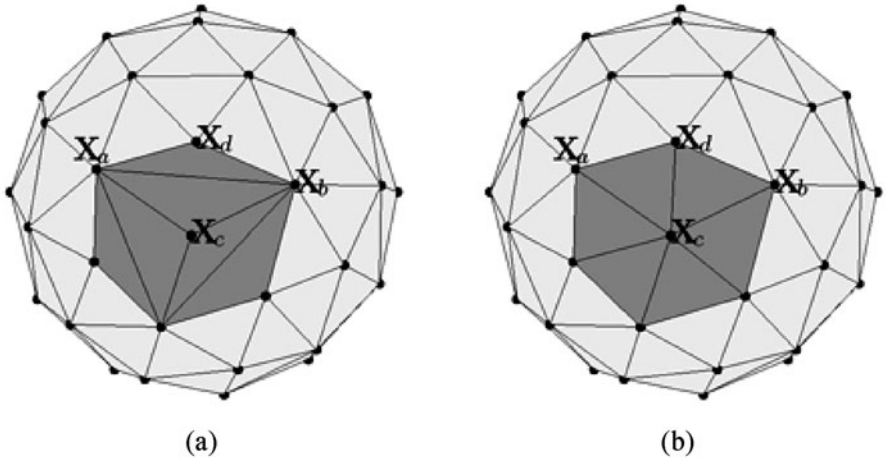

Figure 4. Schematic illustration of the flipping algorithm.

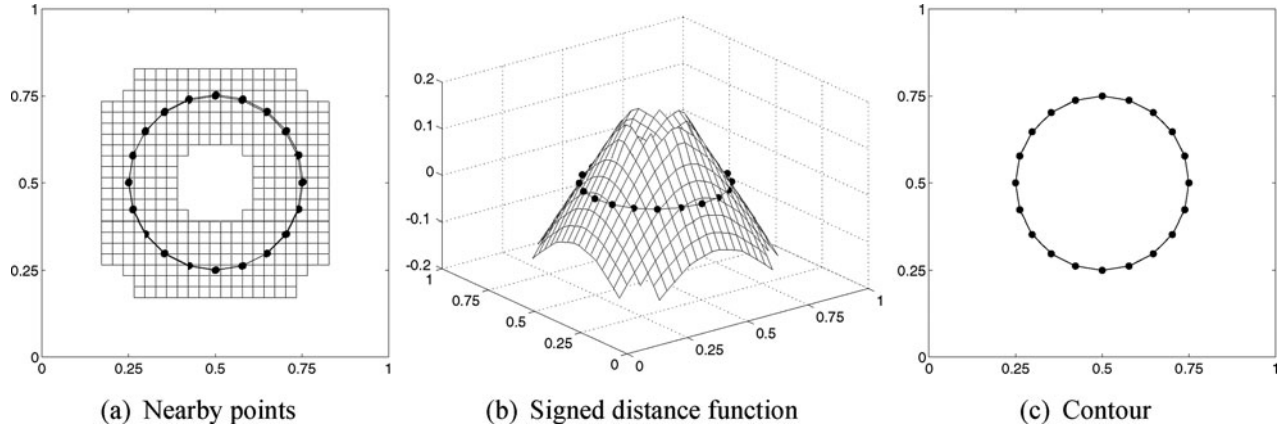

Figure 5. Schematic illustration for constructing a signed distance function by using the surface elements. (a) Nearby points. (b) Signed distance function. (c) Contour.

of points within a band around the evaluated surface (see Figure 5(b)). Figure 5(c) shows the node points and zero contour. The more surface elements there are, the smoother the zero contour of a signed distance function is.

We extend the above algorithm to the three-dimensional case. Suppose one triangular mesh $\mathbf{Tri}_s = (\mathbf{X}_l, \mathbf{X}_m, \mathbf{X}_q)$ on the surface distributes the distance and its orientation to the point $\mathbf{x}_{ijk}$, which is on the Cartesian grid. Now, we describe the formula to find the shortest distance from the point $\mathbf{x}_{ijk}$ to the triangle and denote the point on the triangle as E where the distance is minimum. To simplify the explanation, we define four vectors as follows: $\mathbf{p} = \overrightarrow{\mathbf{x}_{ijk}E}$, $\mathbf{q} = \overrightarrow{\mathbf{x}_{ijk}\mathbf{X}_m}$, $\mathbf{v}_1 = \overrightarrow{\mathbf{X}_m\mathbf{X}_l}$ and $\mathbf{v}_2 = \overrightarrow{\mathbf{X}_m\mathbf{X}_q}$. Then, we can describe the vector on the triangular mesh by the parameters α and β as follows: $\mathbf{p} - \mathbf{q} = \alpha\mathbf{v}_1 + \beta\mathbf{v}_2$, where $0 \le \alpha + \beta \le 1$, $\alpha \ge 0$, and $\beta \ge 0$. Finding the minimum distance from the triangular mesh to point E is equivalent to finding a minimum value of $\|\mathbf{p}\|^2$ (see Figure 6).

We define the distance function between point E and the triangular mesh by

$$f(\alpha, \beta) = \|\mathbf{p}\|^2 = \|\mathbf{v}_1\|^2\alpha^2 + \|\mathbf{v}_2\|^2\beta^2 + \|\mathbf{q}\|^2 + 2\mathbf{v}_1^T\mathbf{v}_2\alpha\beta + 2\mathbf{v}_1^T\mathbf{q}\alpha + 2\mathbf{v}_2^T\mathbf{q}\beta. \quad (8)$$

There are seven potential candidates to be minimum: a critical point, three node points and three boundary points. Note that the function f is a convex function for all α and β since $f_{\alpha\alpha}f_{\beta\beta} - f_{\alpha\beta}^2 > 0$. Therefore, if there is a critical point in the shaded region, f has a minimum value on it.

3.4. *Immersed boundary method*

At the nth time step, we have a velocity field $\mathbf{u}^n$, which is divergence-free, and a surface tension function $\mathbf{f}_{ijk}^n$ calculated by the boundary configuration $\mathbf{X}^n$. An outline

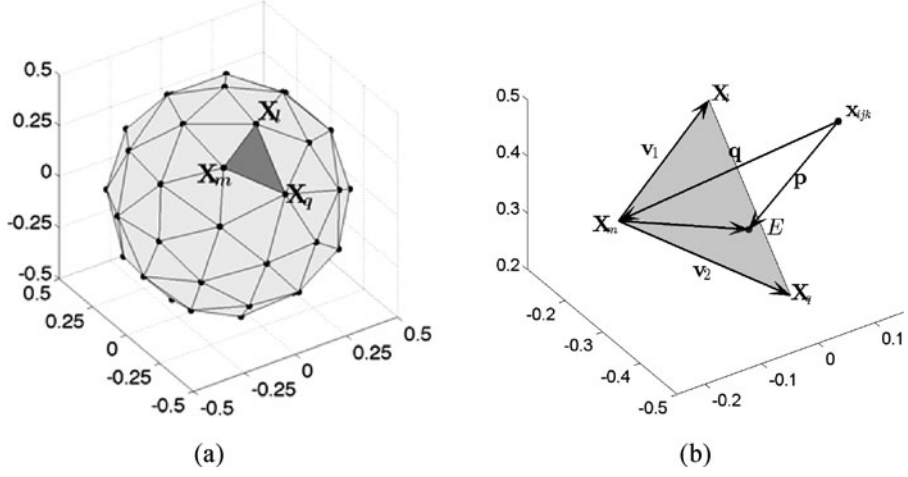

Figure 6. Schematic illustration of the construction of the signed distance function in three dimensions.

of the main procedure in one time step containing the volume correction and remeshing algorithms is as follows:

Step 1. *Surface tension force*

Evaluate the boundary force density $\mathbf{F}_l^n$ from the boundary configuration $\mathbf{X}^n$,

$$\mathbf{F}_l^n = \kappa_l^n \mathbf{n}_l^n, \tag{9}$$

for $l = 1, \ldots, M$, where κ_l^n is the mean curvature and $\mathbf{n}_l^n$ is the normal vector. We then calculate the surface tension force $\mathbf{f}_{ijk}^n$.

$$\mathbf{f}_{ijk}^n = \sum_{l=1}^{M} \mathbf{F}_l^n \delta_h\left(\mathbf{x}_{ijk} - \mathbf{X}_l^n\right)\Delta\mathcal{A}_l, \tag{10}$$

for $i = 1, \ldots, N_x$, $j = 1, \ldots, N_y$ and $k = 1, \ldots, N_z$, where δ_h is a smoothed Dirac delta function (Peskin and McQueen 1995) and $\Delta\mathcal{A}_l$ is a surface area element. The reader could refer to Li et al. (2013) for details of calculations of curvature and normal vector.

Step 2. *Calculation of momentum equation*

The Navier–Stokes Equations (1) and (2) are solved by using a projection method. First, we solve an advection–diffusion equation including surface tension $\mathbf{f}^n$ in the absence of the pressure, resulting an intermediate velocity $\tilde{\mathbf{u}}$,

$$\frac{\tilde{\mathbf{u}} - \mathbf{u}^n}{\Delta t} + \mathbf{u}^n \cdot \nabla_d \mathbf{u}^n = \frac{1}{Re}\Delta \mathbf{u}^n + \frac{1}{We}\mathbf{f}^n \tag{11}$$

where ∇_d and Δ_d denote the centred difference approximations for the gradient and Laplacian operators, respectively. Second, we solve the following equation for the advanced pressure field

$$\frac{\mathbf{u}^{n+1} - \tilde{\mathbf{u}}}{\Delta t} = -\nabla_d p^{n+1}. \tag{12}$$

The pressure p^{n+1} is obtained from the fact that the velocity field is divergence-free at $(n+1)$th time step

$$\Delta_d p^{n+1} = \frac{1}{\Delta t}\nabla_d \cdot \tilde{\mathbf{u}}, \tag{13}$$

where $\nabla_d \cdot$ denotes the discrete divergence operator. The resulting system of Equation (13) is solved using a multigrid method (Trottenberg, Oosterlee, and Schüller 2001). The velocity field $\mathbf{u}^{n+1}$ is then computed by

$$\mathbf{u}^{n+1} = \tilde{\mathbf{u}} - \Delta t \nabla_d p^{n+1}. \tag{14}$$

Step 3. *Updating the interface variables*

The new immersed boundary velocity $\mathbf{U}_l^{n+1}$ and position $\mathbf{X}_l^{n+1}$

$$\mathbf{U}_l^{n+1} = \sum_{i=1}^{N_x}\sum_{j=1}^{N_y}\sum_{k=1}^{N_z} \mathbf{u}_{ijk}^{n+1}\delta_h\left(\mathbf{x}_{ijk} - \mathbf{X}_l^n\right)h^3, \tag{15}$$

$$\mathbf{X}_l^{n+1} = \mathbf{X}_l^n + \Delta t \mathbf{U}_l^{n+1}, \quad l = 1, \ldots, M. \tag{16}$$

These Steps 1–3 complete the procedure for calculating the fluid velocity $\mathbf{u}^{n+1}$ and boundary position $\mathbf{X}^{n+1}$.

We then apply the volume-conserving algorithm (Li et al. 2013) to $\mathbf{X}^{n+1}$ for keeping the initial volume. In addition, after several time steps, we construct the signed distance function using the immersed boundary surface mesh (Section 3.3) and apply the distance function to the remeshing algorithm (Section 3.2) to maintain the mesh uniformity and quality.

4. Numerical experiments in two dimensions

In this section, we perform numerical experiments in two dimensions. The convergence tests and the comparison with previous results are performed to verify our algorithm. We then investigate the effects of the domain size and initial shape on the droplet evolution. In addition, the steady-state droplet shapes are investigated in details under various conditions.

4.1. Convergence test

We calculate the dimensionless axes L/R and B/R to describe the deformation of the drop (Minale 2008). A drop with radius $R = 0.5$ is located in the centre of the computational domain $\Omega = (-1, 1) \times (-1, 1)$. Other parameters are $\mathrm{Re} = 10$, $Ca = 0.2$ and $\dot{\gamma} = 1$. Figure 7 shows the evolutions of the dimensionless axes and orientation angle with increasing mesh size: 32×32, 64×64, 128×128 and 256×256. Here, we use the time step $\Delta t = 0.1h^2$ depending on the space step size h. With the increase of mesh size, the results become convergent.

We next investigate the effect of the number of marker points on the results. The results are calculated on the domain $(-1, 1) \times (-1, 1)$, where the space step size $h = 1/32$. The initial interface is a circle with radius $R = 0.5$. Let M be the number of marker points, and the marker points are evenly distributed on the interface $2\pi R$ at the initial state. Figure 8 shows droplet shapes with different numbers of marker points in steady state. The increasing number of marker points improves the accuracy of interface presentation, but there is a little difference. Thus, in the following two-dimensional simulations, we will use a moderate value of M defined as the nearest integer number of $2\pi Rm/h$, where m is a integer. A Lagrangian mesh size then approximates to h/m. We will use a modest value of $m = 4$.

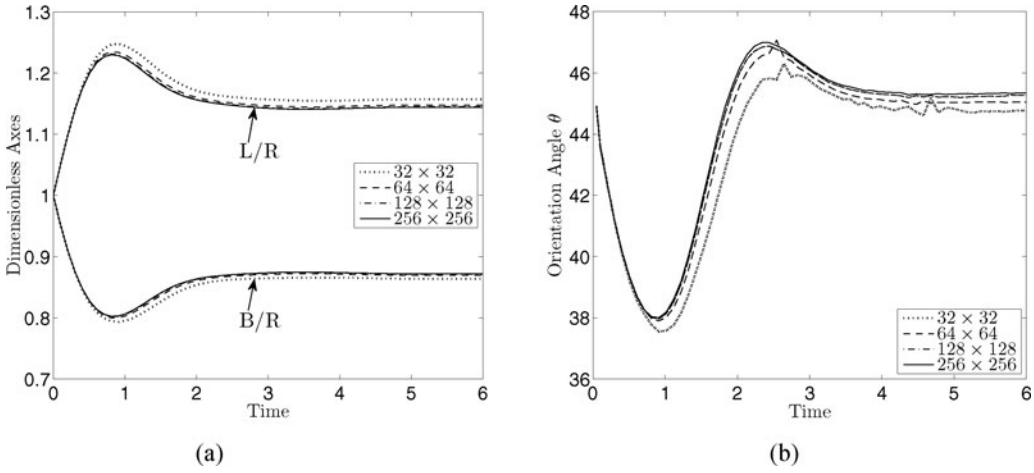

Figure 7. Convergence of (a) dimensionless axes and (b) orientation angle with different mesh sizes.

4.2. Comparison with previous result

We compare our results with previous results (Sheth and Pozrikidis 1995). In Sheth and Pozrikidis (1995), a 24×24 mesh grid is used on the domain $(-1, 1) \times (-1, 1)$. For comparison, we choose a 32×32 mesh with the same parameters. Figure 9 shows the deformation number D as a function of time with different Reynolds and capillary numbers. Our results agree well with those of the previous studies.

4.3. Effect of the domain size

We perform simulations with different domain sizes, $(-2H, 2H) \times (-H, H)$, $(-3H, 3H) \times (-H, H)$ and $(-4H, 4H) \times (-H, H)$ where the wall height $H = 1.25R$ and the droplet radius $R = 1$. The parameters $\mathrm{Ca} = 0.25$, $\mathrm{Re} = 1$ $\dot{\gamma} = 1$, and $h = H/128$ are used. The initial interface is a circle with radius $R = 0.5$. Figure 10 shows the drop shapes in steady state with a time step size $\Delta t = 0.1h^2$. Because of the periodic boundary condition, the solutions depend on the

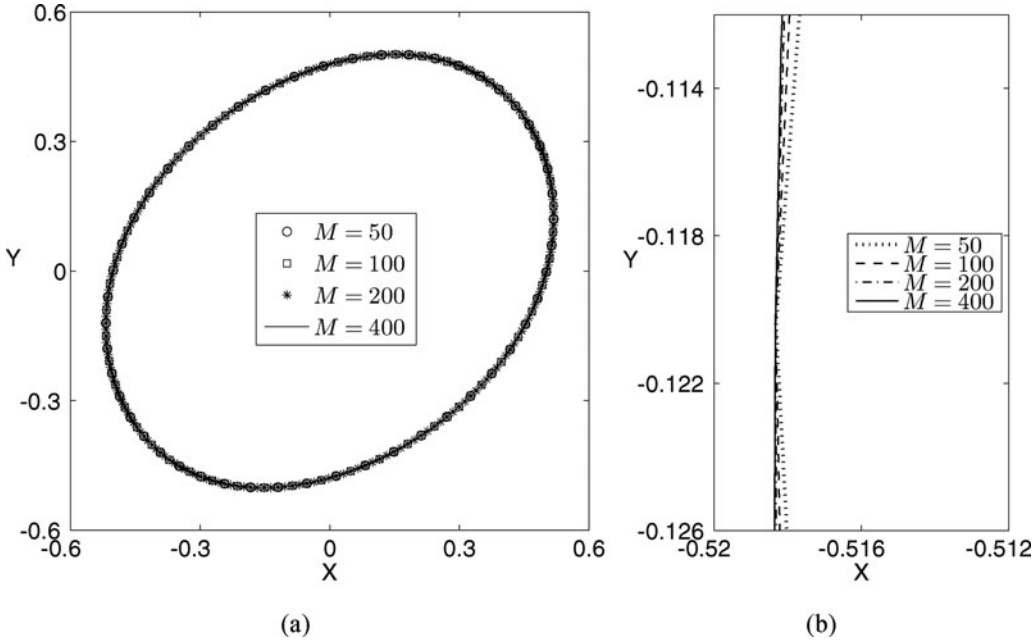

Figure 8. (a) Droplet shape at steady state with different numbers of marker points. (b) Expanded view for different marker points.

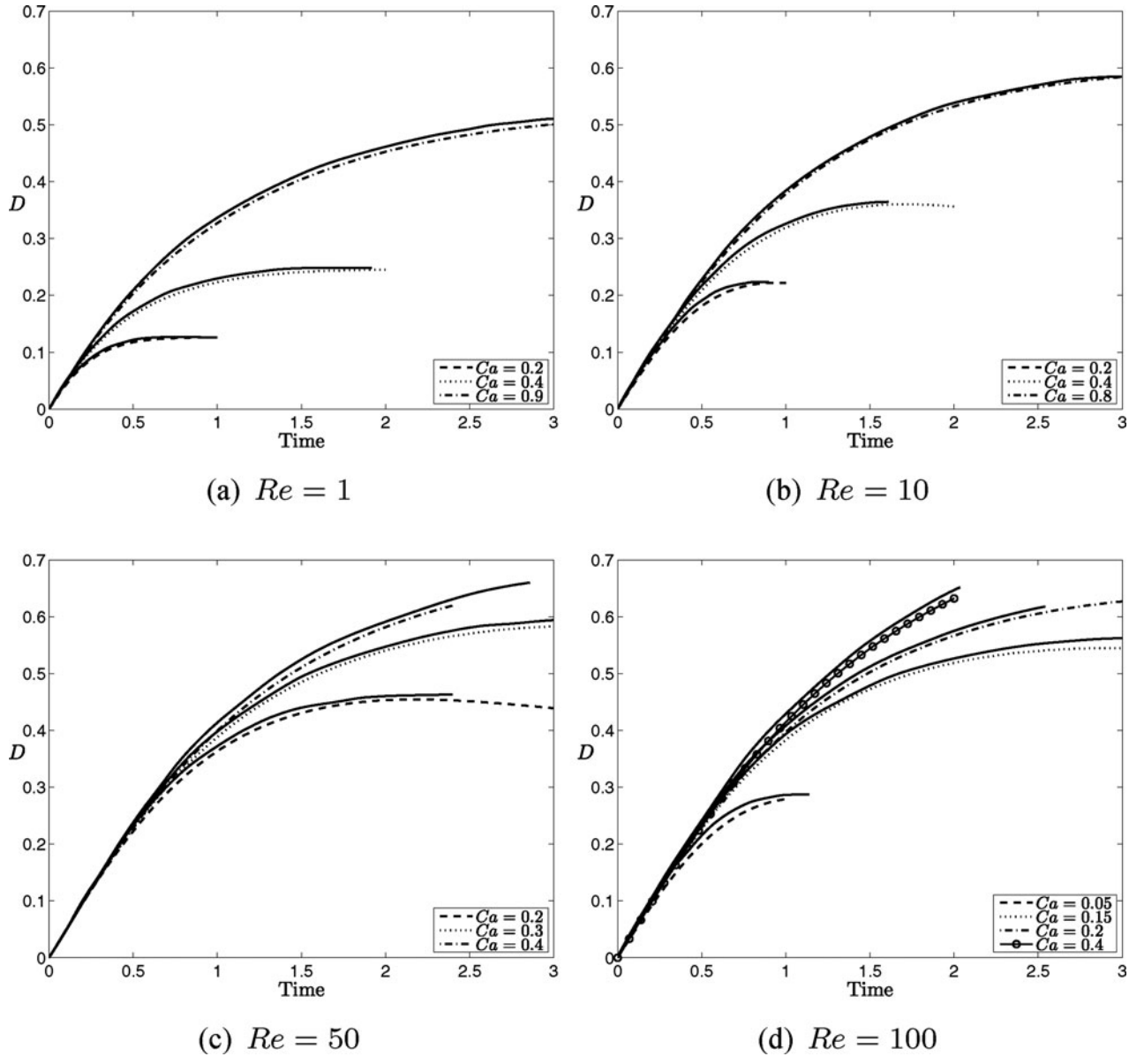

Figure 9. Comparison of the temporal evolution of drop deformation. Solid lines are the results in Sheth and Pozrikidis (1995). (a) Re = 1. (b) Re = 10. (c) Re = 50. (d) Re = 100.

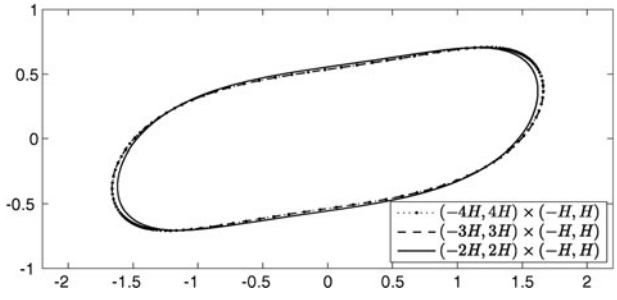

Figure 10. Effect of enlarging the x-direction size on droplet shape in steady state.

x-direction size of the computational domains. However, the droplet shapes obtained on domains $(-3H, 3H) \times (-H, H)$ and $(-4H, 4H) \times (-H, H)$ are almost identical. Therefore, the numerical solution does not change if the x-direction size is large enough.

4.4. *Effect of the initial state*

To show that the steady-state droplet shape is independent of the initial state, we take different initial shapes as shown in Figure 11(a). The three rectangles and the ellipse have the same area π. With space step size $h = 1/32$ and time step

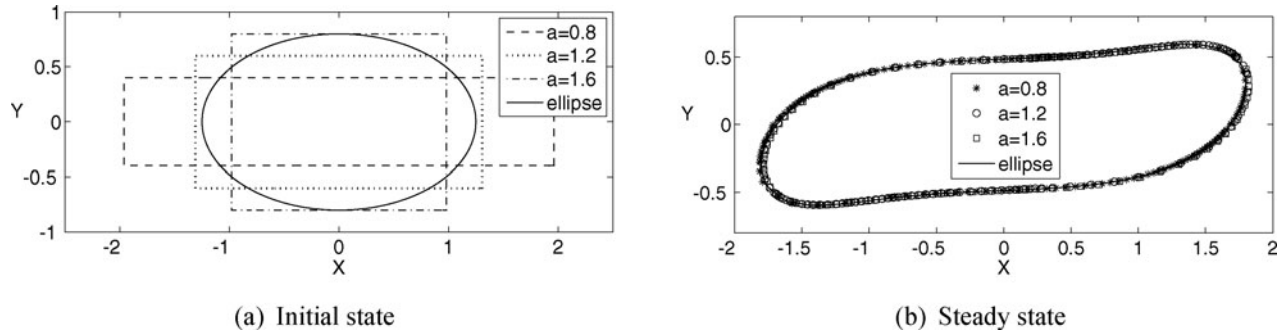

Figure 11. Comparison for different initial configurations having the same area. (a) Initial state. (b) Steady state.

size $\Delta t = 0.1h^2$, numerical solutions are computed on the domain $(-3, 3) \times (-1, 1)$. The other parameters used are $\mathrm{Re} = 1$, $\mathrm{Ca} = 0.25$ and $\dot{\gamma} = 1$. At steady state, the droplet deformations almost overlap (Figure 11(b)).

4.5. *Droplet state with wall confinement*

For the two-dimensional simulations, we set the initial marker points as $\mathbf{X}^0 = (R\cos\alpha, R\sin\alpha)$ if $H > R$, dividing by the Lagrangian size Δs. If $H \leq R$, we use $(R_1\cos\alpha, R_2\sin\alpha)$ for the generation of initial marker points.

We investigate the wall effect by increasing the confinement ratio (see Figures 12 and 13). The calculations are on the domain $(-3H, 3H) \times (-H, H)$ with space step size $h = H/32$. Other parameters used are as follows: $R = 1$, $\mathrm{Re} = 1$, $\mathrm{Ca} = 0.25$, $\dot{\gamma} = 1$ and $\Delta t = 0.1h^2$.

Figure 12 shows the deformation of the droplet and velocity vectors at $y = \pm R$ when the droplet is in steady state. As the wall height decreases, the velocity at height $y = \pm 1$ is more straightforward, which means that the wall velocity strongly affects the droplet deformation.

To compare the deformation shapes, we put the results from Figure 12 together (Figure 13(a)). We observe that the drop is elongated and inclines toward the horizontal axis gradually with increasing confinement ratio. Figure 13 shows the droplet deformations with the smaller wall height. The initial droplets are the ellipses, which have the same area π. The droplet shapes become more stretched and extruded as the wall height decreases.

Figure 14 shows the droplet shapes at steady state with wall height $H = 0.7R$ and different Re and Ca numbers. The calculations are on the domain $(-4H, 4H) \times (-H, H)$ with space step size $h = H/32$. Other parameters are used as follows: $R = 1$, $\dot{\gamma} = 1$ and $\Delta t = 0.1h^2$. Figure 14(a) shows that the droplets get sigmoidally stretched as the Reynolds number increases, and Figure 14(b) shows that droplets become elongated as the capillary number increases.

The velocity field of the shear flow makes the drop rotate. At steady state, the interface point moves along the interface and returns to its original position periodically (a phenomenon is called tank-treading). We track the interface point and calculate the tank-treading time. We investigate

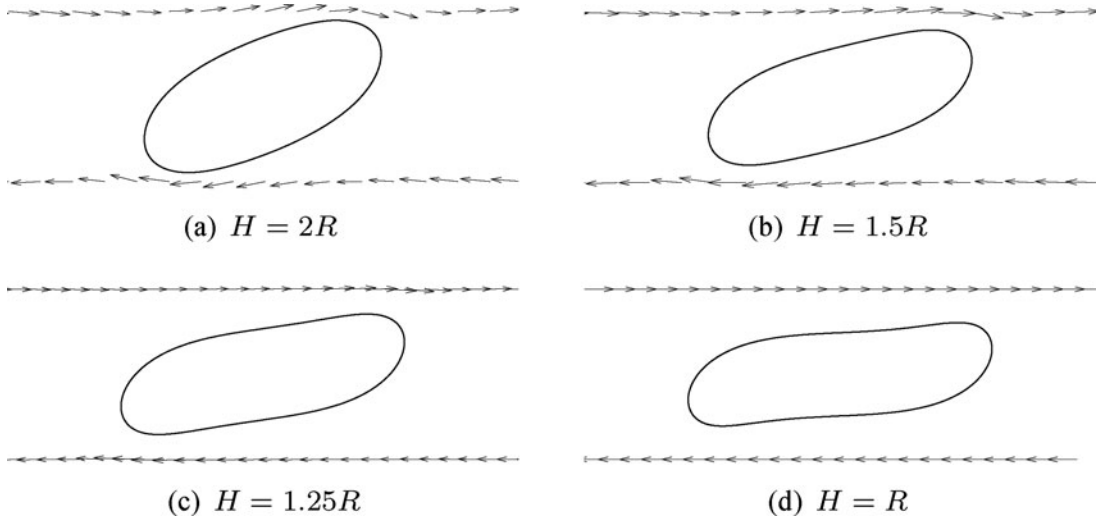

Figure 12. Drop deformation and corresponding velocity vectors at $y = \pm 1$. (a) $H = 2R$. (b) $H = 1.5R$. (c) $H = 1.25R$. (d) $H = R$.

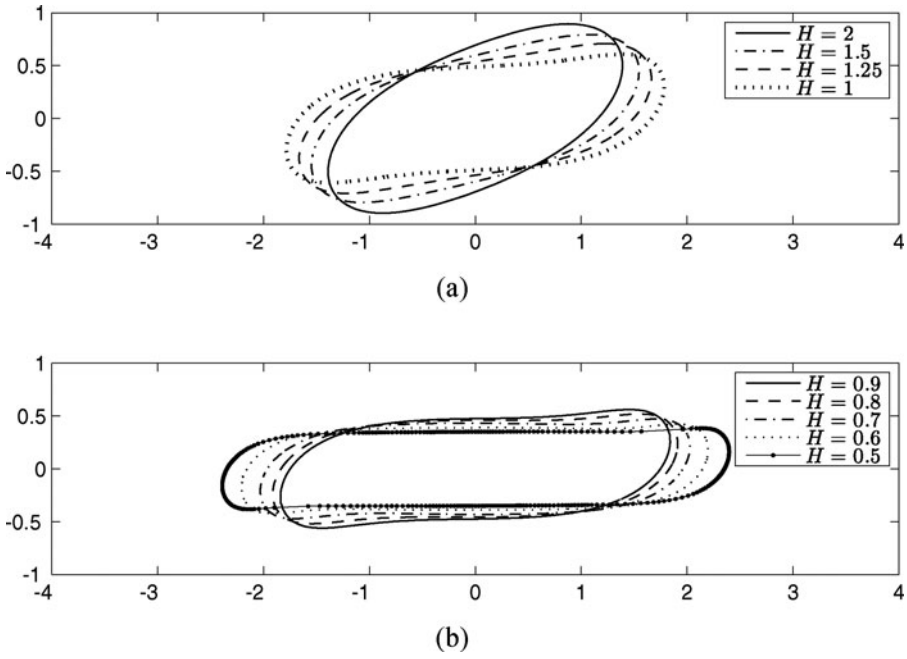

Figure 13. Droplet shapes at steady state with varying wall height.

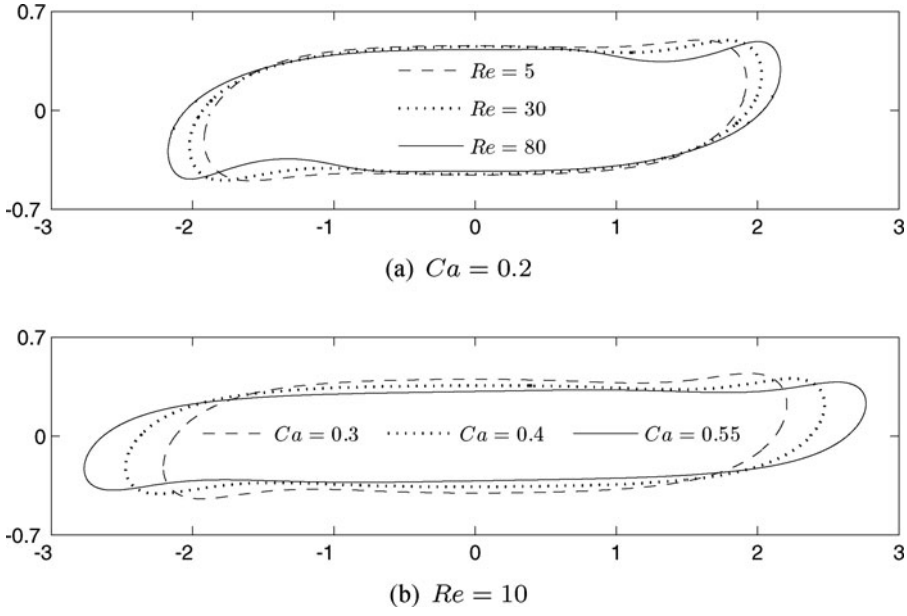

Figure 14. Droplet shapes at steady state with different Re and Ca numbers. (a) Ca = 0.2. (b) $Re = 10$.

the tank-treading time, interface length and arc length at different wall heights H (see Figures 15 and 16). Ca = 0.3, Re = 1 and $\dot{\gamma} = 1$ are used.

Figure 15 shows the tank-treading time and interface length of the droplet at steady state. With the decrease of the wall height, both the tank-treading times and drop interface length increase. There are almost no wall effects on either the tanking-treading time or the interface length when the wall height changes from $2H$ to $3H$.

Figure 16 shows the arc length of the tank-trading curve that covers one time period at different wall heights. The speed of the tank-treading point, which is the slope of the arc length, changes periodically.

5. Numerical experiments in three dimensions

In this section, we investigate the wall confinement effect in three dimensions. We first show the effect of the mesh grid

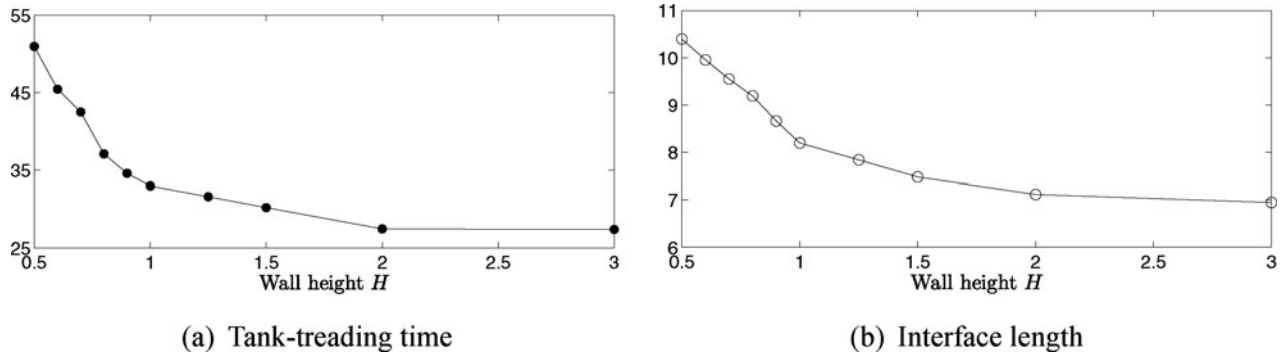

Figure 15. (a) Tank-treading time and (b) interface length of the droplet versus wall height in steady state. (a) Tank-treading time. (b) Interface length.

size and the number of interface points. A comparison of with and without remeshing algorithm is performed to illustrate the necessity of using the remeshing procedure. We then study the droplet state in the confined wall by comparing with the experimental data and theoretical values. Finally, we show the effect of Re and Ca numbers on the droplet shape for the more confined wall height.

For the three-dimensional simulations, we generate initial marker points as a sphere using the DistMesh algorithm for the surface mesh if $R < H$. If $H = R$, we use an ellipsoid that has the same volume as the sphere, $4\pi R^3/3$.

5.1. *Effect of mesh size and the number of marker points*

We investigate the effect of the mesh grid size and the number of marker points. For the initial condition, the spherical droplet with radius $R = 0.5H$ is centred at (0, 0, 0) in the computational domain $\Omega = (-2H, 2H) \times (-2H, 2H) \times (-H, H)$. We use the parameter values as $\mathrm{Re} = 1$, $\mathrm{Ca} = 0.3$ and $\dot{\gamma} = 1$. We calculate to time $t = 2$ with the time step $\Delta t = 0.1h^2$. Figure 17 shows the droplet shapes with different mesh grid size with the fixed number of marker points $M = 1287$. There is no evident difference between two droplet shapes. We next fix the mesh grid as $64 \times 64 \times 32$ and use the same parameters above mentioned except the number of marker points. Figure 18 shows that there is little difference by increasing the number of marker points.

5.2. *Necessity of remeshing*

The remeshing algorithm plays an important role on the long time simulation. We compare the droplet evolution with and without remeshing algorithm in conjunction with the volume correction procedure. We calculate to time $t = 10$ with $\Delta t = 0.1h^2$. Other parameters $\mathrm{Re} = 1$, $\mathrm{Ca} = 0.3$ and $\dot{\gamma} = 1.5$ are used. Without remeshing procedure, neither with nor without volume correction could maintain marker points well distributed (Figure 19(a) and (b)). At time $t = 5$, the marker points concentrate near to the tip sections, and at a longer time $t = 10$, the surface points distorted in the middle of droplet. However, the droplet shape keeps well with a remeshing procedure (Figure 19(c)).

5.3. *Droplet state with wall confinement*

For the following simulations, we use the number of marker points $M = 1827$ for the sphere with radius R and $M = 1894$ for the ellipsoid of which the z-directional semiaxis is $0.8R$. We use $R = 1$, $h = H/16$, and $\Delta t = 0.1h^2$. The computational domain is $(-2H, 2H) \times (-2H, 2H) \times (-H, H)$, if not specified.

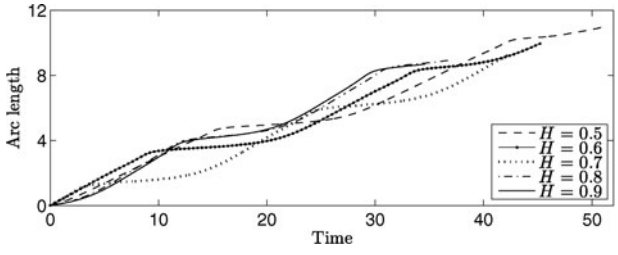

Figure 16. Arc length of the tank-treading point with varying wall height.

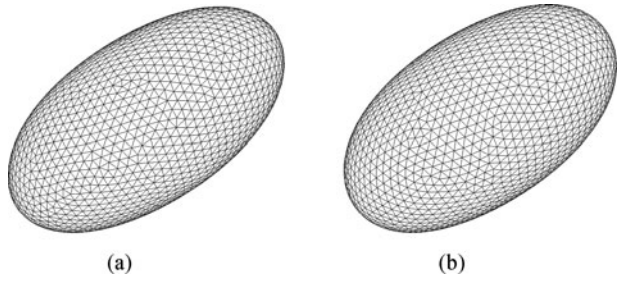

Figure 17. Droplet shape at time $t = 2$ with (a) $64 \times 64 \times 32$ and (b) $128 \times 128 \times 64$ mesh grids.

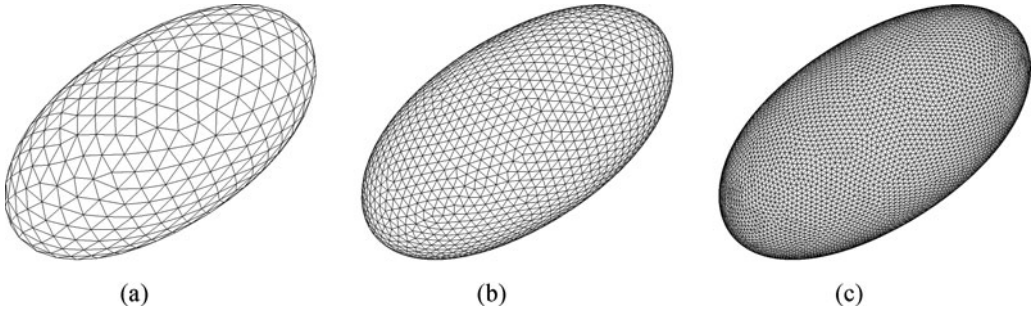

Figure 18. Droplet shape at time $t = 2$ with the number of interface marker points M being (a) 480, (b) 1827 and (c) 7518.

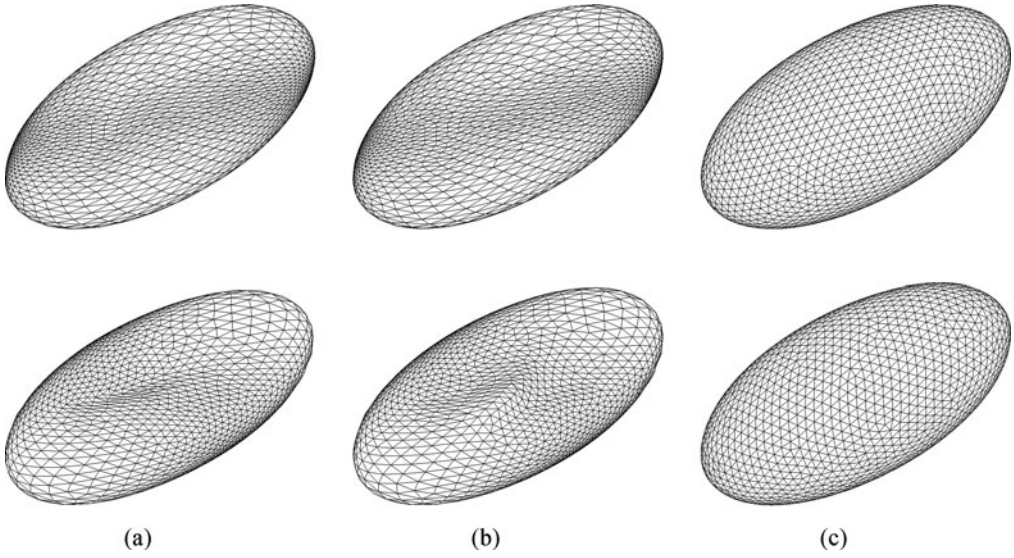

Figure 19. Droplet deformation with (a) without remeshing and without volume correction procedure, (b) without remeshing and with volume correction procedure and (c) with remeshing and with volume correction procedure. First and second rows are at time $t = 5$ and 10, respectively.

We compare our results with two theoretical models in Shapira and Haber (1990) and Minale (2008) and experimental results in Vananroye, Van Puyvelde, and Moldenaers (2007). We use wall height $H = 1.2R$. For the other parameters, $Re = 1$ and $\dot{\gamma} = 1.2$ are used. We measure the dimensionless axes L/R, B/R and W/R with different Ca numbers. Figure 20 shows a comparison among the model predictions, experimental results, and our simulations. Our

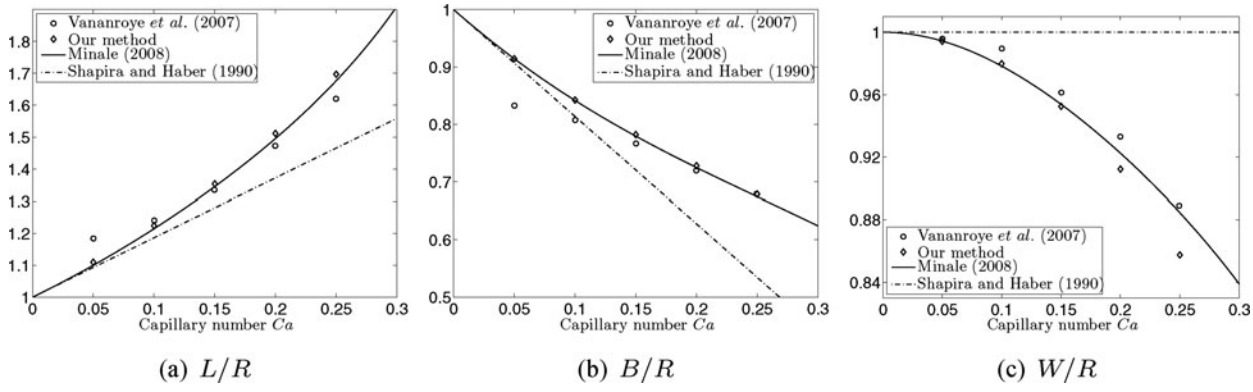

Figure 20. Dimensionless axes of the droplet at steady state versus Ca number. Note that in theoretical and experimental references, $\lambda = 1.07$, whereas in our simulation, $\lambda = 1$. (a) L/R. (b) B/R. (c) W/R.

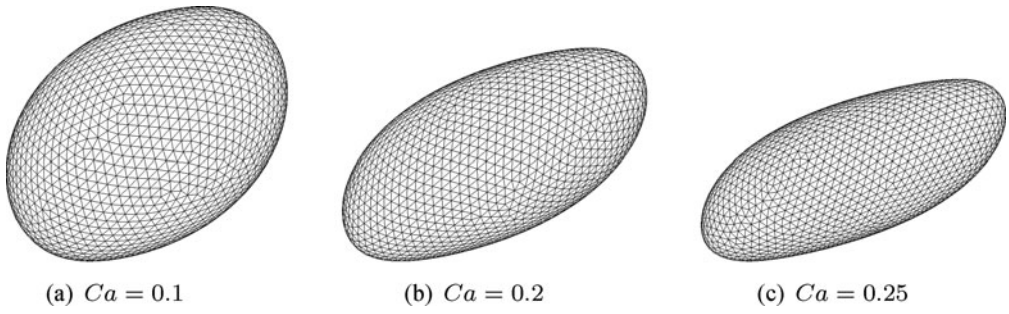

Figure 21. Droplet shape at steady state in a side view at different Ca numbers. (a) $Ca = 0.1$. (b) $Ca = 0.2$. (c) $Ca = 0.25$.

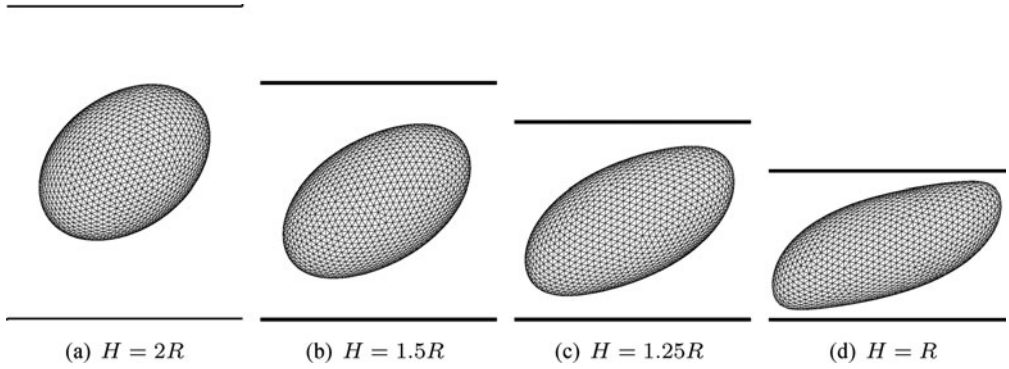

Figure 22. Droplet shapes at steady state with different wall heights in three dimensions. (a) $H = 2R$. (b) $H = 1.5R$. (c) $H = 1.25R$. (d) $H = R$.

simulations show good agreements with the Minale model and experimental results.

Figure 21 shows the simulations of droplet shape at steady state in the x-z plane. The reader could refer to Vananroye et al. (2008) for a comparison with experimental results. The wall height $H = 1.2R$, Re $= 1$ and $\dot{\gamma} = 1.2$ are used. The simulation results agree well with experimental results at the three different capillary numbers.

We furthermore perform simulations to investigate the effect of the wall height as in two-dimensional cases. Figure 22 shows the droplet shapes at steady state with different wall heights. The other parameters used are Re $= 1$,

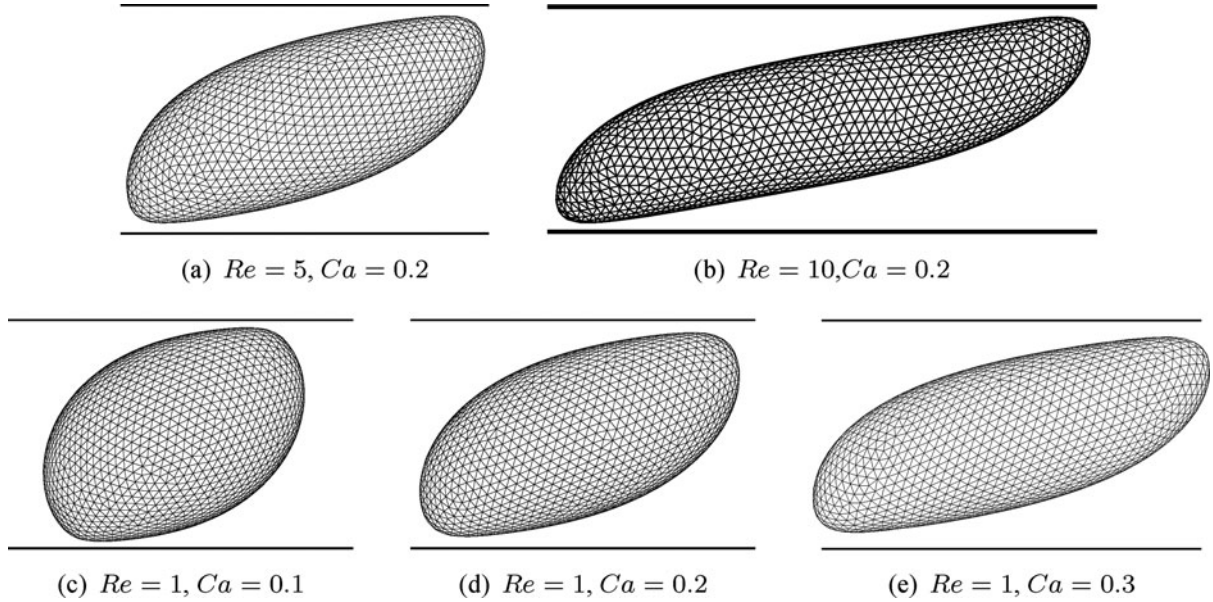

Figure 23. Droplet shape at steady state with different Re and Ca numbers in three dimensions. (a) Re $= 5$, Ca $= 0.2$. (b) Re $= 10$, Ca $= 0.2$. (c) Re $= 1$, Ca $= 0.1$. (d) Re $= 1$, Ca $= 0.2$. (e) Re $= 1$, Ca $= 0.3$.

Table 1. Dimensionless axes of the droplet at steady state for the cases shown in Figure 23. The Reynolds number is Re = 1.

Ca	0.1	0.2	0.3
L/L_{ini}	1.145	1.380	1.670
B/B_{ini}	1.005	0.882	0.793
W/W_{ini}	0.882	0.826	0.736

Ca = 0.25 and $\dot{\gamma} = 1$. With the increase of confinement ratio, the droplet become elongated and develops a sigmoidal shape similar to that in the two-dimensional case (see Figure 12). However, the droplet deformations in three dimensions are less elongated than those in two dimensions.

Figure 23 shows the steady state with different Re and Ca numbers. The droplet becomes more elongated along the fluid flow with increasing Re and Ca. Here, $H = R$ and $\dot{\gamma} = 1$ are used. We set the domain as $\Omega = (-4H, 4H) \times (-2H, 2H) \times (-H, H)$.

To show the relative change of the steady-state droplet, we define the dimensionless axes in the cases of wall height $H > R$, as L/L_{ini}, B/B_{ini} and W/W_{ini}, where L_{ini}, B_{ini} and W_{ini} are the semiaxes for the initial ellipsoidal shape. Table 1 shows the values of these dimensionless axes at different Ca numbers corresponding to the shapes in Figures 23(c)–23(e). The values of dimensionless axes that are greater than 1 tell us that the droplet is inflated in that axis direction whereas the values that are less than 1 show that the droplet is contracted in that axis direction.

6. Conclusions

We numerically investigated droplet dynamics under shear flow between two parallel plates by the IBM in two and three dimensions. A surface remeshing algorithm coping with the distortion of interface points was described. Furthermore, it was shown that this remeshing procedure takes an important role in long time simulations for droplet deformation. We validated our numerical method by comparing with experimental results and theoretical models and good agreements were obtained. Moreover, higher confinement ratio cases with elliptically initial shape in two and three dimensions were presented to show the droplet dynamics. Our numerical method confirmed that the droplet confined by two parallel walls presents different behaviours compared with unconfined ones under shear flow and there is an increase of droplet elongation with sigmoidal shape and greater orientation to the flow direction.

Acknowledgements

This research was supported by the Basic Science Research Program through the National Research Foundation of Korea (NRF) funded by the Ministry of Education, Science and Technology (No. 2011-0023794). The authors also wish to thank the reviewers for their constructive and helpful comments on the revision of this article.

References

Ardekani, A.M., S. Dabiri, and R.H. Rangel. 2009. "Deformation of a Droplet in a Particulate Shear Flow." *Physics of Fluids* 21 (9): 093302-1–093302-8.

Cardinaels, R., S. Afkhami, Y. Renardy, and P. Moldenaers. 2011. "An Experimental and Numerical Investigation of the Dynamics of Microconfined Droplets in Systems with One Viscoelastic Phase." *Journal of Non-Newtonian Fluid Mechanics* 166: 52–62.

Ceniceros, H.D., R.L. Nos, and A.M. Roma. 2010. "Three-Dimensional, Fully Adaptive Simulations of Phase-Field Fluid Models." *Journal of Computational Physics* 229 (17): 6135–6155.

Chaffey, C.E., and H. Brenner, 1967. "A Second-Order Theory for Shear Deformation of Drops." *Journal of Colloid and Interface Science* 24 (2): 258–269.

Cristini, V., S. Guido, A. Alfani, J. Blawzdziwicz, and M. Loewenberg. 2003. "Drop Breakup and Fragment Size Distribution in Shear Flow." *Journal of Rheology* 47 (5): 1283–1298.

Cristini, V., and Y. Renardy. 2006. "Scalings for Droplet Sizes in Shear-Driven Breakup: Non-Microfluidic Ways to Monodisperse Emulsions." *Fluid Dynamics & Materials Processing* 2: 77–93.

Garstecki, P., H.A. Stone, and G.M. Whitesides. 2005. Mechanism for Flow-Rate Controlled Breakup in Confined Geometries: A Route to Monodisperse Emulsions. *Physical Review Letters* 94 (16): 164501-1–164501-4.

Griggs, A.J., A.Z. Zinchenko, and R.H. Davis. 2007. "Low-Reynolds-Number Motion of a Deformable Drop Between Two Parallel Plane Walls." *International Journal of Multiphase Flow* 33 (2): 182–206.

Gueyffier, D., J. Li, A. Nadim, R. Scardovelli, and S. Zaleski. 1999. "Volume-of-Fluid Interface Tracking With Smoothed Surface Stress Methods for Three-Dimensional Flows." *Journal of Computational Physics* 152 (2): 423–456.

Harlow, F.H., and J.E. Welch. 1965. "Numerical Calculation of Time-Dependent Viscous Incompressible Flow With Free Surface." *Physics of Fluids* 8 (12): 2182–2189.

Janssen, P.J.A., and P.D. Anderson. 2007. "Boundary-Integral Method for Drop Deformation Between Parallel Plates." *Physics of Fluids* 19 (4): 043602-1–043602-11.

Kim, J.S. 2005. "A Continuous Surface Tension Force Formulation for Diffuse-Interface Models." *Journal of Computational Physics* 204 (2): 784–804.

Li, Y., E. Jung, W. Lee, H.G. Lee, and J. Kim. 2012. "Volume Preserving Immersed Boundary Methods for Two-Phase Fluid Flows." *International Journal for Numerical Methods in Fluids* 69 (4): 842–858.

Li, Y., A. Yun, D. Lee, J. Shin, D. Jeong, and J. Kim. 2013. "Three-Dimensional Volume-Conserving Immersed Boundary Model for Two-Phase Fluid Flows." *Computer Methods in Applied Mechanics and Engineering* 257: 36–46.

Minale, M. 2008. "A Phenomenologiacal Model for Wall Effects on the Deformation of an Ellipsoidal Drop in Viscous Flow." *Rheologica Acta* 47: 667–675.

Minale, M. 2010. "Models for the Deformation of a Single Ellipsoidal Drop: A Review." *Rheologica Acta* 49: 789–806.

Persson, P.-O. 2006. "Mesh Size Functions for Implicit Geometries and PDE-Based Gradient Limiting." *Engineering with Computers* 22: 95–109.

Persson, P.-O., and G. Strang. 2004. "A Simple Mesh Generator in MATLAB." *SIAM Review* 46 (2): 329–345.

Peskin, C.S. 1977. "Numerical Analysis of Blood Flow in the Heart." *Journal of Computational Physics* 25 (3): 220–252.

Peskin, C.S., and D.M. McQueen. 1995. "A General Method for the Computer Simulation of Biological Systems Interacting With Fluids." *Symposia of the Society for Experimental Biology* 49: 265–276.

Pillapakkam, S.B., and P. Singh. 2001. "A Level-Set Method for Computing Solutions to Viscoelastic Two-Phase Flow." *Journal of Computational Physics* 174 (2): 552–578.

Rallison, J.M. 1984. "The Deformation of Small Viscous Drops and Bubbles in Shear Flows." *Annual Review of Fluid Mechanics* 16: 45–66.

Renardy, Y. 2007. The Effects of Confinement and Inertia on the Production of Droplets. *Rheologica Acta* 46 (4): 521–529.

Renardy, Y.Y., and V. Cristini. 2001. "Effect of Inertia on Drop Breakup Under Shear." *Physics of Fluids* 13 (1): 7–13.

Shapira, M. and S. Haber. 1988. "Low Reynolds Number Motion of a Droplet Between Two Parallel Plates." *International Journal of Multiphase Flow* 14 (4): 483–506.

Shapira, M., and S. Haber. 1990. "Low Reynolds Number Motion of a Droplet in Shear Flow Including Wall Effects." *International Journal of Multiphase Flow* 16 (2): 305–321.

Sheth, K.S., and C. Pozrikidis. 1995. "Effects of Inertia on the Deformation of Liquid Drops in Simple Shear Flow." *Computers & Fluids* 24 (2): 101–119.

Sibillo, V., G. Pasquariello, M. Simeone, V. Cristini, and S. Guido. 2006. "Drop Deformation in Microconfined Shear Flow." *Physical Review Letters* 97 (5): 054502-1–054502-4.

Stone, H.A. 1994. "Dynamics of Drop Deformation and Breakup in Viscous Flows." *Annual Review of Fluid Mechanics* 26: 65–102.

Taylor, G.I. 1932. "The Viscosity of a Fluid Containing Small Drops of Another Fluid." *Proceedings of the Royal Society A* 138: 41–48.

Taylor, G.I. 1934. "The Formation of Emulsions in Definable Fields of Flow." *Proceedings of the Royal Society A* 146: 501–523.

Thorsen, T., R.W. Roberts, F.H. Arnold, and S.R. Quake. 2001. "Dynamic Pattern Formation in a Vesicle-Generating Microfluidic Device." *Physical Review Letters* 86 (18): 4163–4166.

Tice, J.D., A.D. Lyon, and R.F. Ismagilov. 2004. "Effects of Viscosity on Droplet Formation and Mixing in Microfluidic Channels." *Analytica Chimica Acta* 507 (1): 73–77.

Trottenberg, U., C.W. Oosterlee, and A. Schüller. 2001. *Multigrid*. San Diego: Academic.

Tucker III, C.L., and P. Moldenaers. 2002. "Microstructural Evolution in Polymer Blends." *Annual Review of Fluid Mechanics* 34: 177–210.

Vananroye, A., P.J.A. Janssen, P.D. Anderson, P.V. Puyvelde, and P. Moldenaers. 2008. "Microconfined Equiviscous Droplet Deformation: Comparison of Experimental and Numerical Results." *Physics of Fluids* 20 (1): 013101-1–013101-10.

Vananroye, A., P. Van Puyvelde, and P. Moldenaers. 2006a. "Effect of Confinement on Droplet Breakup in Sheared Emulsions." *Langmuir* 22 (9): 3972–3974.

Vananroye, A., P. Van Puyvelde, and P. Moldenaers. 2006b. "Morphology Development During Microconfined Flow of Viscous Emulsions." *Applied Rheology* 16 (5): 242–247.

Vananroye, A., P. Van Puyvelde, and P. Moldenaers. 2007. "Effect of Confinement on the Steady-State Behavior of Single Droplets During Shear Flow." *Journal of Rheology* 51 (1): 139–153.

Xu, J.J., Z. Li, J. Lowengrub, and H. Zhao. 2006. "A Level-Set Method for Interfacial Flows With Surfactant." *Journal of Computational Physics* 212 (2): 590–616.

Yue, P., J.J. Feng, C. Liu, and J. Shen. 2004. "A Diffuse-Interface Method for Simulating Two-Phase Flows of Complex Fluids." *Journal of Fluid Mechanics* 515: 293–317.

Yue, P., C. Zhou, J.J. Feng, C.F. Ollivier-Gooch, and H.H. Hu. 2006. "Phase-Field Simulations of Interfacial Dynamics in Viscoelastic Fluids Using Finite Elements With Adaptive Meshing." *Journal of Computational Physics* 219 (1): 47–67.